Research Square

Preprints are preliminary reports that have not undergone peer review.
They should not be considered conclusive, used to inform clinical practice,
or referenced by the media as validated information.

Probabilistic Prioritization of Human Health Outcomes Associated with Microplastic Exposure: A Reliability-Inspired Mathematical Framework Integrating Monte Carlo Analysis

Masoumeh Khamehchi
Universidad Ecotec
Rafael Luque
Universidad Ecotec
Umberto Cornelli
Loyola University Chicago
Claudio Casella
icarocus@gmail.com

University of Pavia Department of Chemistry: Universita degli Studi di Pavia Dipartimento di Chimica
https://orcid.org/0000-0002-1806-4825

Research Article

Keywords: Microplastics, environmental epidemiology, probabilistic modeling, hypothesis-generating framework

Posted Date: November 25th, 2026

DOI: https://doi.org/10.21203/rs.3.rs-11429895/v1

License: This work is licensed under a Creative Commons Attribution 4.0 International License.
Read Full License

Probabilistic Prioritization of Human Health Outcomes Associated with Microplastic Exposure: A Reliability-Inspired Mathematical Framework Integrating Monte Carlo Analysis

Masoumeh Khamehchi [1], Rafael Luque, Ph.D.[1,2], Dr. Umberto Cornelli, MD. Ph.D.[3], and Claudio Casella, Ph.D.[4*],

[1]Universidad ECOTEC, Km 13.5 Samborondón, Samborondón EC092302, (Ecuador); mkhamehchi@gmail.com; rluque@ecotec.edu.ec

[2]Peoples Friendship University of Russia (RUDN University), 6 Miklukho Maklaya Str., Moscow, 117198, (Russian Federation). luke-r@pfur.ru

[3]Department of Molecular Pharmacology and Therapeutics, School of Medicine, Loyola University, Chicago, IL 60660, (USA); ucornelli@gmail.com

[4]Department of Chemistry, University of Pavia, Viale Taramelli 12, 27100, Pavia (Italy); claudio.casella01@universitadipavia.it

*Corresponding author:

Dr. Claudio Casella, Ph.D.

Department of Chemistry

University of Pavia

Viale Taramelli 12, 27100, Pavia (ITALY)

claudio.casella01@universitadipavia.it

ABSTRACT

Human exposure to microplastics and nanoplastics (MNPs) is ubiquitous, yet a quantitative framework to evaluate the internal consistency of hypothesized symptom clusters is lacking. This study introduces an exploratory probabilistic framework to prioritize clinical manifestations within a literature-derived symptom-disease matrix, providing a novel mathematical approach for environmental health prioritization. We constructed a binary matrix of 26 manifestations across 40 diseases via the Chicago Cluster Evaluation System. Non-linear logistic curve fitting, 10,000 Monte Carlo simulations, limit-state reliability formulations (β), and sensitivity analyses were applied. The logistic model showed high goodness-of-fit (R^2=0.9852). Following Bonferroni correction (α=0.0019), ultrasound modifications and bloating/bowel habit demonstrated robust above-baseline significance ($P_{neg}\approx$0.0000, β=4.75), while four features showed nominal significance ($P_{neg}<$0.05). This framework does not establish an MNP-associated phenotype or attributable risk. Instead, it provides a robust, hypothesis-generating tool to guide future prospective epidemiological investigations with quantified internal MNP burdens.

Keywords: *Microplastics; environmental epidemiology; probabilistic modeling; hypothesis-generating framework.*

Abbreviations: ADME-T: Absorption, Distribution, Metabolism, Excretion, and Toxicity; ALT/AST: Acute Serum Transaminase Elevations; BBB: Blood-Brain Barrier; BPA: Bisphenol-A; CCES: Chicago Cluster Evaluation System; CRP: C-reactive protein; ECHA: European Chemicals Agency; EDCs: Endocrine-Disrupting Chemicals; FORM: First-Order Reliability Method; HBGVs: Health-Based Guidance Values; hs-CRP: C-Reactive Protein; LPS: Lipopolysaccharides; LSF: Limit State Function; MPs: Microplastics; MSy: Microplastic Syndrome; NPs: Nanoplastics; PBPK: Physiologically Based Pharmacokinetic; PE: Polyethylene; PET: Polyethylene Terephthalate; PK-PD: Pharmacokinetic-Pharmacodynamic; PP: Polypropylene; PRCC: Partial Rank Correlation Coefficients; PS: Polystyrene; PU: Polyurethane; PVC: Polyvinyl Chloride; Py-GC/MS:

Pyrolysis–Gas Chromatography–Mass Spectrometry; RMSE: Root Mean Square Error; ROS: Reactive Oxygen Species; US EPA: United States Environmental Protection Agency; WHO: World Health Organization.

Introduction

Microplastics (MPs) and nanoplastics (NPs) have accumulated in terrestrial, freshwater, and marine ecosystems at an unprecedented rate due to an exponential increase in plastic manufacture over the past 70 years (MacLeod et al., 2021; Plastic Europe 2025; Stoett et al., 2024) As a result, ingestion, inhalation, and skin contact have all increased human exposure to MNPs, rendering them one of the most ubiquitous emerging xenobiotics of the twenty-first century (Casella et al., 2024; Li et al., 2023; Prata et al., 2020). MNPs have been identified in many human tissues, including blood, placenta, liver, kidneys, lungs, reproductive organs, vascular thrombi, and brain tissue, according to recent analytical studies (Casella et al., 2025a; Cornelli et al., 2026; Marfella et al., 2024). These findings have shifted scientific focus toward investigating the potential biological implications of chronic internal exposure rather than solely addressing environmental pollution.

Experimental evidence indicated that MNPs may induce cellular-level alterations such as oxidative stress, mitochondrial dysfunction, chronic inflammation, endocrine disruption, immunological dysregulation, and altered cellular signalling (Casella and Ballaz, 2024; Fan and Ha, 2025). Nonetheless, given that human exposure is broad, persistent, and complex, translating these underlying mechanisms into identifiable clinical symptoms remains a formidable challenge. Building upon the Chicago Cluster Evaluation System (CCES)—an exploratory clinical framework integrating 30 clinical, laboratory, and imaging variables potentially associated with chronic MNP exposure—a recent study recently proposed the hypothesis of a putative Microplastic Syndrome (MSy) (Cornelli et al., 2025). While that study represented a significant conceptual advancement by combining disparate clinical findings into a unified diagnostic hypothesis, the CCES framework remained primarily descriptive and lacked quantitative confirmation.

A critical objective in contemporary environmental medicine is the transition from descriptive clinical observations to rigorous quantitative decision-support models (Li et al., 2025; Wardani et al., 2024). Probabilistic methods capable of handling uncertainty, variability, and non–linear interactions

among multiple variables are increasingly vital in modern risk assessment (Koelmans et al., 2022; Nguyen et al., 2025). Reliability engineering–originally developed for structural safety assessment–has recently found valuable applications in biomedical engineering, clinical risk prediction, and healthcare decision analysis because it acceptable bounds (Kin and Liu, 2020; Liu et al., 2020). Concurrently, Partial Rank Correlation Coefficients (PRCC) provide a robust framework for identifying variables that exert the greatest influence on model behaviour, while Monte Carlo simulation has emerged as a primary method for propagating uncertainty through non–linear models (Chen et al., 2021; Mohammadpour et al., 2023; Zhao et al., 2023).

For the purposes of this study, we adopt the following operational definitions: microplastics (MPs) are defined as solid plastic particles ranging from 1 μm to 5,000 μm in size, whereas nanoplastics (NPs) comprise particles smaller than 1 μm. We acknowledge that MPs and NPs exhibit distinct physicochemical properties, including surface-area-to-volume ratios, biomolecular corona formation, and translocation potentials. In this study, the umbrella term "MNPs" is utilized strictly as a methodological reflection of the current clinical literature, which frequently groups these entities together or relies on indirect chemical proxies (such as plasticizers) rather than direct, size-resolved particle quantification. Our probabilistic framework evaluates the internal statistical consistency of the resulting symptom clusters, rather than the distinct toxicokinetic pathways of specific particle sizes.

The present study introduces an exploratory probabilistic approach that combines non-linear logistic curve fitting, Monte Carlo simulation, a probabilistic limit-state formulation, and global sensitivity analysis, building upon the CCES framework. Crucially, the aim of this study is not to evaluate the existence of a unique clinical syndrome, nor to establish causality or assess attributable risk between MNP exposure and specific health outcomes. Rather, the primary aim is to conduct an exploratory mathematical evaluation of symptom distribution across a selected disease spectrum to assess whether the clinical manifestations previously hypothesized within the CCES framework exhibit Adequate internal quantitative consistency. The underlying dataset consists exclusively of binary indicators of symptom co-occurrence across 40 representative diseases and does not contain individual-level MNP exposure measurements or clinical health-outcome observations. Accordingly, this work serves as an exploratory framework designed to generate hypotheses and guide the design of future

prospective epidemiological studies incorporating quantified internal MNP burdens, rather than providing quantitative confirmation of an MNP-associated clinical phenotype or representing risk attribute to MNPs.

2. Materials and Methods

For this study, the operational definitions differentiate MPs, characterised as solid plastic particles measuring between 1μm and 5,000 μm, from NPs, which are defined as particles less than 1 μm. MNPs demonstrate inherently different physicochemical characteristics, including as surface-area-to-volume ratios, biomolecular corona development, and translocation capabilities. Nonetheless, the existing clinical and analytical literature indicates that direct size-resolved particle detection in human tissues is significantly hindered by technology resolution limitations (i.e., Py-GC/MS and Raman spectroscopy thresholds at the nanoscale). Consequently, studies frequently rely on indirect chemical proxies or group these entities together. Our probabilistic model evaluates the internal statistical consistency of the resulting clinical manifestation clusters, acknowledging that the underlying data sources cannot yet definitively attribute specific symptoms to distinct particle sizes or polymer morphologies.

2.1. Study Design

To assess the internal probabilistic consistency of the hypothesised multisystemic clinical cluster, the current analysis was designed as a quantitative methodological study. It must be explicitly emphasised that the unit of analysis in this study is the disease category, rather than the individual patient. The constructed matrix comprises binary indicators of symptom co-occurrence across representative medical conditions and does not contain individual-level MNP exposure measurements, exposure contrasts, or unexposed control groups. Consequently, this study cannot estimate epidemiological metrics such as odds ratios, relative risks, or attributable fractions. Rather, the analysis is strictly an exploratory mathematical evaluation of symptom distribution across a selected set of diseases, designed to generate hypotheses rather than to establish epidemiological causality. The study was carried out in five phases: (1) identifying clinically significant symptoms associated with human exposure to MNP based on prior clinical evidence; (2) creating a standardised symptom-disease matrix that included common acute and chronic illnesses; (3) modelling symptom incidence mathematically using logistic probability functions; (4) propagating uncertainty through Monte Carlo simulation; and

(5) quantifying symptom resilience using structural reliability engineering and global sensitivity analysis. It is explicitly noted that the unit of analysis in this study is the disease category, not the individual patient. The constructed matrix does not contain individual-level MNP exposure or health-outcome data.

It is explicitly noted that the unit of analysis in this study is the disease category, not the individual patient. Because the dataset lacks individual-level MNP exposure measurements, exposure contrasts, or unexposed control groups, this study cannot estimate epidemiological metrics such as odds ratios, relative risks, or attributable fractions. The analysis is strictly an exploratory mathematical evaluation of symptom distribution across a selected set of diseases.

2.2. Source of Clinical Evidence

The CCES, which gathered the most recent clinical data on possible symptoms clinical variables included in the exploratory CCES framework, provided the clinical dataset used in this study. An organised literature evaluation conducted in accordance with PRISMA 2020 reporting guidelines led to the development of the CCES itself. PubMed, Web of Science, Scopus, and Google Scholar are four electronic databases that were searched for articles from January 2000 to September 2025 (Cornelli et al., 2025).

992 publications were found in the initial search. 140 peer-reviewed human studies that reported clinical, pathological, or biomarker data indicating MNP exposure were collected for qualitative synthesis after title screening, abstract appraisal, and full-text eligibility assessment (**Figure 1**). Instead of doing a second literature search, the current study used the CCES dataset as its verified clinical reference framework.

The symptom-disease matrix was constructed based on the Chicago Cluster Evaluation System (CCES) framework. To ensure methodological transparency, the CCES data extraction followed a structured protocol aligned with PRISMA guidelines. Two independent reviewers screened the literature, extracted data on human clinical manifestations, and resolved discrepancies through consensus. Animal-only or purely mechanistic studies were excluded from the final quantitative matrix. A comprehensive breakdown of the included studies, their evidence type (direct MNP measurement vs.

chemical proxy/biomarker), and risk-of-bias considerations is provided in **Supplementary Material S5 (Table S3-**Studies and Evidence Typology**)**.

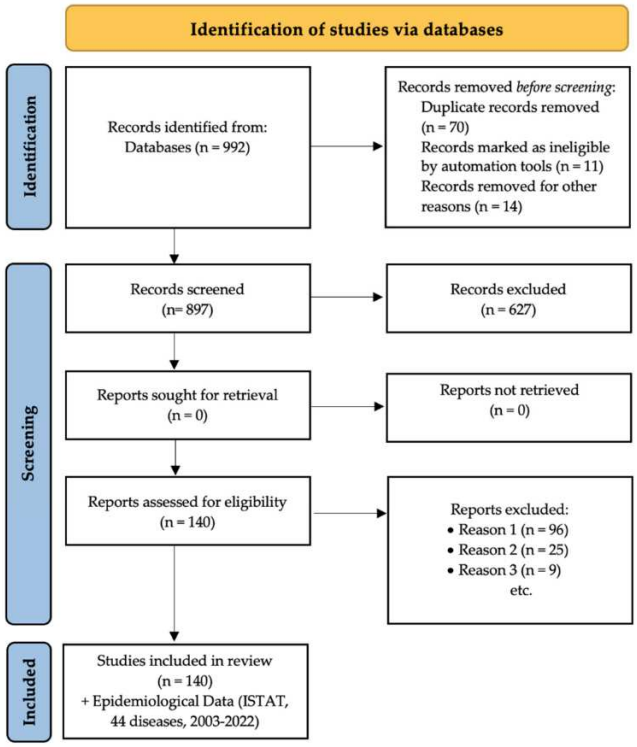

Figure 1. PRISMA 2020 Flow Diagram (*based on Cornelli et al., 2025*).

2.3. Construction of the Symptom–Disease Matrix

The frequency of persistent clinical manifestations among typical human diseases exhibiting clinical overlap with the suggested MNP-related phenotype was represented by a binary symptom-disease matrix. From the supplemental clinical dataset, 40 sample medical conditions including endocrine, gastrointestinal, neurological, respiratory, autoimmune, psychiatric, infectious, haematological, genitourinary, gynaecological, and toxicological disorders were selected.

Disease selection was guided by three criteria: (1) clinical relevance within routine medical practice, (2) the presence of at least six CCES-compatible manifestations, and (3) the availability of standardized diagnostic descriptions in internationally recognized medical references (specifically Robbins and Cotran Pathologic Basis of Disease, Harrison's Principles of Internal Medicine, and the Merck Manual). Each disease was independently evaluated for the presence or absence of every CCES

variable, yielding a total of 1,040 binary observations. Across 40 diseases and 26 clinical manifestations ($x_{i,j}$= 1 if symptom *j* was reported in disease *i*, and $x_{i,j}$= 0 otherwise).

It is critical to address the potential risk of circularity and selection bias introduced by the criterion requiring at least six CCES–compatible manifestations, as this threshold deliberately enriches the matrix for multisystemic overlap. To rigorously evaluate whether the identification of core manifestations is an artifact of this selection process or an independent property of the matrix, a stratified "Leave–One–Class–Out" (LOCO) sensitivity analysis was performed (detailed in Supplementary Material S2, Figure S3). By systematically re-running the entire probabilistic framework while excluding entire disease classes (i.e., all neurological or all infectious conditions), we demonstrated that core manifestations—such as persistent fatigue, abdominal pain, and gastrointestinal alterations—consistently maintained a probability of negative deviation (P_{neg}) well below the 0.50 threshold across all exclusion scenarios (stability ≥ 90%). This confirms that the core symptom prioritization is a robust, emergent feature of the broader multisystemic disease spectrum rather than a trivial consequence of circular disease selection.

2.4. Variable Harmonization

Prior analysis, a number of clinical symptoms described under different nomenclature in the literature were harmonised in order to remove semantic duplication while maintaining important medical information. Specifically, a single variable called Cognitive Impairment was created by combining concepts such "cognitive alterations," "cognitive impairment," and "cognitive dysfunction." Similarly, increased C-reactive protein (CRP) and systemic inflammatory markers were categorised under Inflammatory Biomarkers, while "behavioural alterations," "behavioural changes," and "psychiatric manifestations" were included under Behavioural Alterations. A final standardised dataset with 26 discrete variables reflecting laboratory findings, clinical symptoms, and imaging abnormalities was obtained as a result of this harmonisation procedure.

2.5. Estimation of Symptom Frequency

Each clinical manifestation's occurrence frequency (f_i) was computed as $f_i = n_i / N$, where N=40 is the total number of diseases examined and n_i is the number of disorders displaying symptom *i*. The

198 resultant observed frequencies, which represent the incidence of each symptom just within the selected
199 disease spectrum rather than throughout the whole population, serve as empirical descriptors of the
200 internal consistency of the suggested clinical phenotype.

201 *2.6. Nonlinear Logistic Curve Fitting for Symptom Frequency Distribution*

202 To establish an empirical baseline distribution of symptom frequencies, a nonlinear logistic curve
203 fitting procedure was applied to the rank-ordered data. The objective function minimized the Sum of
204 Squared Residuals (SSR) between the observed frequencies N_i and the model predictions $f(x_i)$ using
205 the Levenberg-Marquardt optimization algorithm (implemented via scipy.optimize.curve_fit). The
206 optimization was initialized with starting values of $L = 30$, $k = 0.5$, and $x_0 = 10$, and constrained to
207 ensure mathematically plausible parameters ($L > 0,\ k > 0$). The 95% confidence intervals for the
208 parameters were derived from the diagonal of the resulting covariance matrix. The full covariance matrix
209 is provided in Supplementary Material S4.

210 A decreasing logistic function was implemented to describe the distribution of clinical symptoms
211 among the 40 disorders examined in this study. The non-linear, monotonic decay pattern observed in
212 symptom frequency data, where symptoms are rated according to their prevalence across the illness
213 spectrum, led to the selection of the logistic model. The expression for the mathematical formulation is:
214 **Eq 1.**

215 $$f(x; L; k;\ x_0) = \frac{L}{1 + \exp[\mathrm{k}(\mathrm{x} - x_0)]}$$

216 Where *f(*x) represents the predicted frequency of a symptom at rank position *x*. *L* denotes the
217 asymptotic maximum frequency (upper bound). *k* is the steepness parameter governing the rate of decay.
218 x_0 represents the inflection point (rank at which the function reaches *L*/2).

219 Nonlinear logistic curve fitting was selected to establish an empirical baseline distribution
220 because it naturally constrains outcomes within the [0,1] interval, provides stable mathematical behavior
221 for sparse datasets, and facilitates subsequent uncertainty propagation through Monte Carlo simulation.
222 The model goodness-of-fit was comprehensively evaluated through residual analysis, the coefficient of
223 determination (R^2), and the root mean square error (RMSE).

It is important to clarify the scale of the model evaluation. The reported coefficient of determination (R^2=0.9852) and Root Mean Square Error (RMSE=0.9138) were calculated on the raw count scale (frequencies ranging from 0 to 40). An RMSE of 0.9138 on this scale indicates that the model predicts the number of diseases exhibiting a symptom with an average error of less than one disease. Supplementary analyses confirm that fitting the model on a proportion scale (0 to 1) yields mathematically equivalent results, with an identical R2R2 (0.9852), a proportionally scaled RMSE (0.0228), and identical shape parameters (kk and x0x0), as detailed in **Supplementary Material S3**.

2.7. Monte Carlo Simulation (Uncertainty Quantification)

Given the inherent uncertainty in model parameter estimation, a Monte Carlo probabilistic analysis was conducted to propagate parameter uncertainty through the predictive framework. The covariance matrix of the estimated parameters $(\widehat{L}, \widehat{k}, \widehat{x}_0)$ was extracted from the optimization procedure, and parameter samples were drawn from a multivariate normal distribution: **Eq. 2**

$$\begin{pmatrix} L \\ k \\ x_0 \end{pmatrix} \sim \mathcal{N}\left(\begin{pmatrix} \hat{L} \\ \hat{k} \\ \hat{x}_0 \end{pmatrix}, \Sigma\right)$$

where Σ represents the covariance matrix capturing both parameter variances and their cross-correlations. A total of 10,000 Monte Carlo iterations were performed, with each iteration generating a unique parameter set and corresponding predicted symptom frequencies. To ensure physical meaningfulness of the logistic function, parameter samples yielding negative values for *L* (asymptote) or *k* (steepness) were excluded from the analysis, as these would violate the mathematical constraints of a decreasing logistic curve. This filtering step typically removes less than 1% of samples when the covariance matrix is well-conditioned.

In order to explicitly depict uncertainty generated by clinical heterogeneity, medical condition variability, measurement error, and symptom categorisation, Monte Carlo simulation was implemented. The consequent ensemble produced empirical confidence intervals for every model output by repeated sampling, guaranteeing a solid foundation for assessing model stability under parameter modification.

It is important to note that this Monte Carlo procedure propagates only the uncertainty associated with the fitted logistic parameters (L, k, x_0). It does not account for epistemic uncertainties related to

disease selection, symptom ascertainment, binary coding decisions, terminology harmonization, or study-level heterogeneity. Therefore, the resulting confidence intervals represent parameter uncertainty bounds rather than comprehensive uncertainty estimates that capture all sources of variability in the underlying evidence base.

2.8. Probabilistic Classification Framework

To systematically classify symptoms based on their deviation from the empirical baseline, a mathematical limit-state function was formulated as $g_i = N_i - f(x_i)$. It is crucial to emphasize that this formulation is a purely statistical transformation used for probabilistic classification and does not imply physical failure, biological robustness, clinical protection, or any specific biological property. The structural engineering analogies of 'resistance' and 'load' have been intentionally omitted to avoid misleading physical interpretations. Symptoms with $gi \geq 0$ (Above-baseline domain) exhibit frequencies higher than the model prediction, while those with $gi < 0$ (Below-baseline domain) fall below the expected frequency.

$$g_i = N_i - f(x, L, k, x_0)$$

Where g_i is the limit state function value for symptom *i*. N_i represents the observed frequency (resistance term, constant for each symptom). $f(x, L, k, x_0)$ represents the model-predicted frequency (load term, variable under uncertainty).

The classification of clinical manifestations into core or below- Baseline manifestations were based on the sign of the limit state function g_i for each symptom i. A symptom was classified as a core manifestation of the emerging microplastic syndrome when $g_i \geq 0$, indicating that its observed frequency across the 40 diseases analyzed equals or exceeds the frequency predicted by the logistic model. This condition implies that the symptom is more prevalent than expected under the baseline distribution, suggesting it exhibits a higher prevalence than the baseline expectation for generic multisystemic diseases. This mathematical prioritization identifies the symptom as a candidate marker worthy of targeted investigation in future prospective MNP cohorts, rather than implying it is a biologically evaluated defining feature of the syndrome. Conversely, a symptom was classified as a peripheral manifestation when $g_i < 0$, indicating that its observed frequency falls below the model prediction. Such symptoms, while potentially present in certain disease contexts, do not demonstrate the statistical

robustness required to be considered defining features of the core syndrome. This probabilistic classification framework enables a quantitative distinction between syndrome-defining symptoms and disease-specific or incidental manifestations, thereby providing a reproducible criterion for identifying the clinical phenotype associated with microplastic exposure. This formulation enables probabilistic classification by evaluating the probability of negative deviation (P_{neg}), defined as the likelihood that a symptom's observed frequency is statistically indistinguishable from or lower than the model prediction: **Eq. 4**

$$P_{f,i} = P(g_i < 0) = P(N_i < f(x; L, k, x_0))$$

In the Monte Carlo simulation, the parameters (L, k,x_0) were sampled from a multivariate normal distribution defined by the optimized estimates and their covariance matrix. We formally evaluated the risk of post-sampling truncation bias (i.e., rejecting samples where $L < 0$ or $k < 0$). Given the optimized parameters ($L = 40.07 \pm 6.32,\ k = 0.1589 \pm 0.0147$), the theoretical probability of generating negative values is negligible ($P_L < 10^{-10}$, $P_k < 10^{-27}$). Consequently, the empirical rejection rate in our 10,000 iterations was 0.00%, confirming that the post-sampling distributions remain perfectly normal and free of truncation artifacts. Furthermore, the observed frequencies (N_i) were treated as fixed, deterministic inputs; uncertainty associated with the literature-derived counts themselves was not propagated, representing a conservative estimate of total uncertainty.

The probability of negative deviation was estimated empirically from the Monte Carlo simulations: **Eq. 5**

$$\hat{P}_{f,i} = \frac{1}{N_{sim}} \sum_{j=1}^{N_{sim}} \mathbb{I}\left(g_{i,j} < 0\right)$$

where N_{sim}= 10,000 represents the number of Monte Carlo iterations, and $I(.)$ is the indicator function. The 95% confidence interval for $P_{neg}$was computed using the normal approximation to the binomial distribution: **Eq. 6**

$$CI_{95\%} = \widehat{P_{neg}} \pm 1.96 \sqrt{\frac{\hat{P}_f\left(1 - \hat{P}_f\right)}{N_{sim}}}$$

The clinical phenotype was characterised in this study as a complex system composed of several interrelated symptoms. Every symptom provides a probabilistic contribution to the phenotype's overall reliability. Reliability Engineering analyses the collective behaviour of symptoms rather than assessing each one separately.

It is important to clarify that this formulation is a mathematical analogy borrowed from reliability engineering to facilitate probabilistic classification, rather than a literal physical or biological model. The terms resistance N_i and load $f(x_i)$ are used here in a purely abstract mathematical sense to distinguish observed frequencies from model-predicted frequencies. Unlike classical structural reliability, where resistance and load represent physically independent quantities, both N_i and $f(x_i)$ in this study are derived from the same symptom-disease matrix. Therefore, this framework should be interpreted as a reproducible mathematical tool for prioritizing clinical manifestations based on their deviation from an empirical baseline, rather than as a biophysical model of system failure.

2.9. Standardized Classification Index

To provide a symmetric, dimensionless metric for comparing the probabilistic classification of symptoms, a Standardized Classification Index (β) was computed by transforming the Probability of Negative Deviation (P_{neg}) through the inverse standard normal cumulative distribution function: Eq. 7. This transformation is an arbitrary mathematical standardization procedure that converts probabilities into a symmetric scale to facilitate cross-symptom comparison; it does not represent a structural reliability assessment or possess direct clinical meaning.

$$\beta_i = -\Phi^{-1}\left(P_{f,i}\right)$$

where Φ^{-1} denotes the inverse of the standard normal cumulative distribution function.

The Standardized Classification Index (β) offers several distinct advantages for the probabilistic classification of clinical manifestations. First, it provides a symmetric and intuitive interpretation, where positive values ($\beta > 0$) indicate above-Baseline manifestations and negative values ($\beta < 0$) denote peripheral manifestations, thereby establishing a clear dichotomy between syndrome-defining and secondary features. Second, the magnitude of β carries direct clinical significance, as higher absolute values reflect greater statistical confidence in the symptom's classification, enabling researchers to

prioritize the most robust phenotypic markers. Third, the dimensionless and standardized nature of the Standardized Classification Index facilitates cross-study comparability, allowing for meaningful integration of findings across different symptom categories, organ systems, and clinical domains. In the present analysis, symptoms were classified as core manifestations of the emerging microplastic syndrome when the probability of negative deviation fell below the critical threshold (P_{neg}< 0.5, equivalently β> 0), indicating that the observed frequency statistically exceeds the model prediction with greater than 50% probability under parameter uncertainty.

Structural reliability analysis was quantified via the Standardized Classification Index β, where higher β values indicate greater robustness of symptom classification under parameter uncertainty. Reliability levels were categorized as high robustness (β> 3.0), moderate robustness ($2.0 \leq \beta \leq 3.0$), and low robustness (β< 2.0). These thresholds align with conventional Reliability Engineering standards and provide an intuitive quantitative measure of classification confidence.

It is important to clarify that this transformation is a mathematical standardization procedure that converts probabilities into a symmetric, dimensionless scale, rather than a conventional First-Order Reliability Method (FORM) analysis as practiced in structural reliability engineering. In classical FORM, the Standardized Classification Index represents the minimum distance from the origin to the limit state surface in standard normal space, requiring identification of the design point. Our approach simply transforms the empirically estimated probability of negative deviation (obtained from Monte Carlo simulation) into a standardized metric. The term 'Standardized Classification Index' is used here in a purely abstract mathematical sense to facilitate probabilistic classification and cross-symptom comparison, not to imply structural reliability assessment or biophysical system analysis.

2.10. Global Sensitivity Analysis via PRCC

The PRCC was used in a global sensitivity study to determine which model parameters have the greatest impact on symptom categorisation. PRCC is especially useful for models with correlated inputs considering that, in contrast to simple correlation measures, it quantifies the independent effect of each input parameter on the output while accounting for the influence of other factors. For each symptom i_i, the PRCC for a given parameter θ_j (where $\theta \in \{L, k, x_0\}$) was computed through a systematic

procedure. Initially, a rank transformation was applied by converting both the sampled input parameters θ_j and the corresponding output limit state function values g_i into ranks, utilizing an average ranking method to appropriately handle any tied values. Subsequently, residual computation was performed for each parameter θ_j by regressing its ranks against the ranks of all other input parameters, thereby isolating its unique variance. Finally, the partial correlation was determined by calculating the Pearson correlation coefficient between the resulting residuals of θ_j and the corresponding residuals of g_i. This approach effectively controls for the confounding influence of inter-parameter correlations, enabling the precise quantification of each logistic parameter's independent contribution to the uncertainty in symptom classification.

Mathematically, the PRCC is expressed as:

$$PRCC_j = corr\left(e_{\theta_j}, e_{g_i}\right)$$

where $e_{\theta j}$ and e_{gi} are the residuals from the rank-based regression models.

Global sensitivity analysis was performed using PRCC to quantify the influence of individual parameters on the system's output. Variables exhibiting absolute PRCC values greater than 0.50 (|PRCC|> 0.50) were classified as highly influential. This approach identifies the clinical manifestations that contribute most strongly to overall model reliability, thereby establishing a data-driven basis for prioritizing future clinical validation efforts.

2.11. Statistics Software

All statistical analyses were performed using Python 3.12 (Python Software Foundation, Wilmington, DE, USA). Numerical computations were conducted using *NumPy*, data manipulation was performed with pandas, statistical analyses were carried out using *SciPy* and statsmodels, regression modeling and performance evaluation were implemented with scikit-learn, and graphical outputs were generated using *Matplotlib*.

To guarantee total reproducibility, deterministic computational scripts were employed for all analyses. Upon reasonable request, the whole symptom-disease matrix, simulation methods, and

intermediate datasets are capable of being published, thereby enabling independent validation and further development of the suggested probabilistic framework.

3. Results

3.1. Clinical Dataset and Terminology Harmonization

The final dataset encompassed 40 representative diseases across neurological, endocrine, gastrointestinal, respiratory, cardiovascular, autoimmune, infectious, psychiatric, and toxicological conditions. Following the harmonization of clinical terminology to eliminate semantic redundancy, 26 recurrent clinical manifestations were retained for quantitative evaluation. This yielded a binary symptom–disease matrix containing 1,040 observations. The observed symptom frequencies exhibited marked heterogeneity across the spectrum. Compared to localised organ-specific data, constitutional, neurological, and systemic inflammatory symptoms were observed in a significantly more significant percentage of diseases, suggesting a common multisystemic clinical pattern. The basis for further probabilistic modelling was this empirical distribution.

3.2. Logistic Model Fitting and Parity Analysis

A non-linear logistic curve fitting method was utilised to determine an empirical baseline distribution of recorded symptom frequencies (N). The logistic model exhibited a substantial coefficient of determination ($R^2 = 0.9852$) and a minimal Root Mean Square Error (RMSE = 0.9138) across all 26 clinical presentations. Significantly, this elevated R^2 value indicates the internal mathematical coherence of applying a smooth three-parameter monotonic decay curve to a rank-ordered dataset, rather than demonstrating a non-random biological structure or validation of clinical phenotypes.

To rigorously justify the logistic function as an empirical baseline and evaluate potential overfitting, comparative model fitting and permutation analyses were conducted (Supplementary Material S1 and S2). As detailed in Table S1 (Comparative performance metrics for alternative functional forms fitted to the rank-ordered symptom frequency distribution) and Figure S1, the logistic model achieved superior parsimony relative to alternative decay models (Linear: $R^2= 0.9193$, AIC= 43.38; Power Law: $R^2= 0.9647$, AIC= 23.89; Exponential: $R^2= 0.9819$, AIC= 6.58; Logistic: $R^2= 0.9852$,

AIC= 1.31, BIC= 5.09). Furthermore, a 1,000-iteration permutation test (Figure S2) confirmed that the observed R^2 was statistically distinct from random chance ($p < 0.0001$, permuted mean $R^2 = 0.0575 \pm 0.0634$), confirming that the monotonic decay pattern provides a statistically robust empirical baseline for subsequent limit-state analysis.

The optmised parameters for the logistic baseline function is the following:

$$f(x; L, k, x_0) = \frac{L}{1 + \exp\big(k(x - x_0)\big)}$$

where the estimate is L = 40.07 ± 6.32 (asymptotic maximum frequency), k = 0.159 ± 0.015 (decay steepness), and x_0 = 4.21 ± 2.03 (inflection rank).

The steepness parameter k was estimated with high precision (relative error < 10%), whereas the larger standard error associated with x_0 reflects the inherent uncertainty in pin-pointing the inflection point within a 26-variable dataset. The parity (N) and model-predicted (f(x)) frequencies is presented in **Figure 2**. The limit state function boundary g= 0 is defined by the dashed diagonal line (N= f(x)). Potential symptoms of core syndrome are points above the border (g> 0) where observed frequencies surpass model projections. Peripheral characteristics are represented by points below (g< 0).

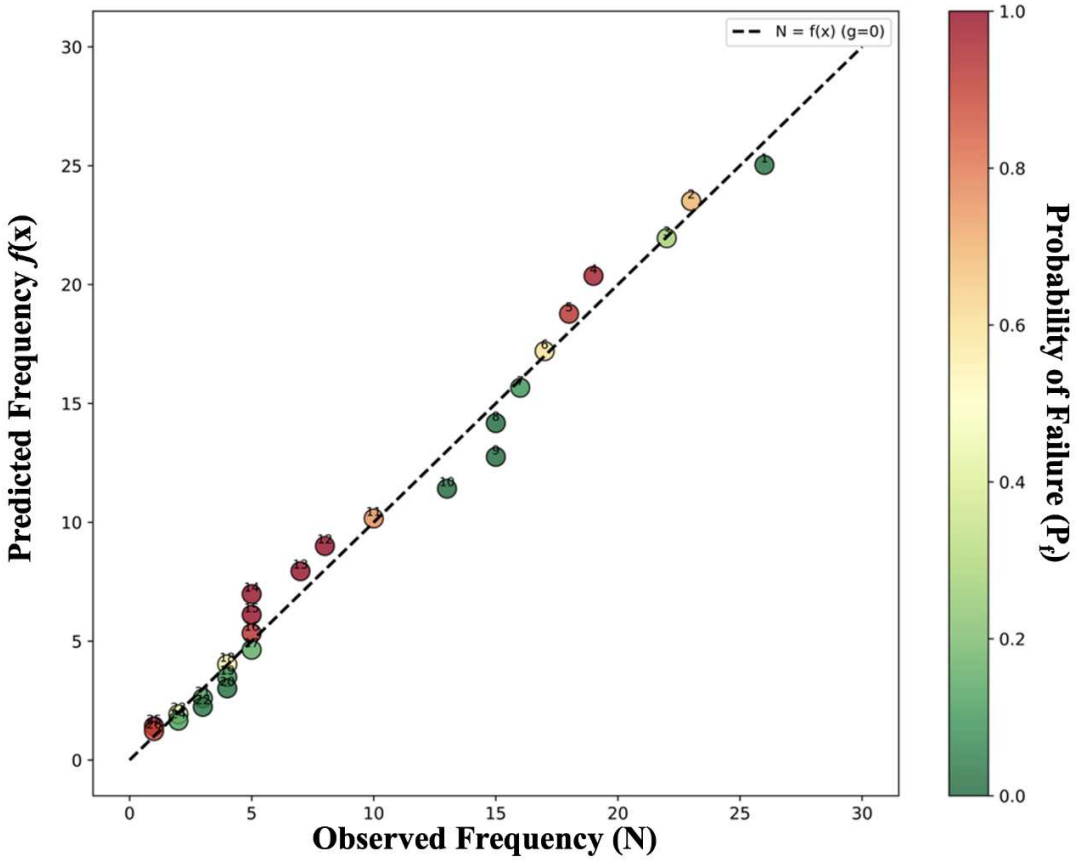

Figure 2. Parity plot of observed versus logistic model-predicted frequencies across 26 clinical manifestations. The dashed diagonal line denotes the identity relationship (N=f(x), g= 0). Data points are color-coded by their probability of negative deviation (P_{neg}), ranging from green ($P_{neg}\approx 0$, core symptoms) to red ($P_{neg}\approx 1$, Below-Baseline manifestations), with numerical labels indicating symptom rank (1–26).

3.2.1. Model Comparison and Statistical Validation of the Logistic Baseline

To rigorously justify the selection of the logistic function as the empirical baseline distribution and to address concerns regarding potential overfitting to rank-ordered data, two supplementary analyses were conducted.

Model Comparison Using Information Criteria: The logistic model was compared against three alternative functional forms: linear, exponential, and power-law decay models. Model performance was evaluated using the coefficient of determination (R^2), root mean square error (RMSE), and information criteria (Akaike Information Criterion [AIC] and Bayesian Information Criterion [BIC]), which penalize model complexity and provide a robust framework for model selection. As summarized in Table S1 and visualized in Figure S1, the logistic model demonstrated superior performance across all metrics:

- Logistic model: $R^2 = 0.9852$, RMSE = 0.9138, AIC = 1.31, BIC = 5.09
- Exponential model: $R^2 = 0.9819$, RMSE = 1.0113, AIC = 6.58, BIC = 10.36
- Power-law model: $R^2 = 0.9647$, RMSE = 1.4105, AIC = 23.89, BIC = 27.66
- Linear model: $R^2 = 0.9193$, RMSE = 2.1325, AIC = 43.38, BIC = 45.90

The logistic model exhibited the lowest AIC and BIC values, indicating it provides the best trade-off between goodness-of-fit and model parsimony. The substantially higher AIC values for the linear (43.38) and power-law (23.89) models confirm that these simpler functional forms fail to adequately capture the monotonic decay pattern observed in the symptom frequency distribution. While the exponential model achieved a comparable R^2 (0.9819), its higher AIC (6.58) and BIC (10.36) relative to the logistic model indicate inferior performance when accounting for model complexity.

Permutation Test for Statistical Significance: To verify that the high R^2 value (0.9852) was not a trivial artifact of fitting a smooth curve to rank-ordered data, a permutation test was conducted. The observed

symptom frequencies were randomly shuffled 1,000 times, and the logistic model was re-fitted to each permuted dataset. The distribution of R^2 values from these random permutations (mean $R^2 = 0.0575 \pm 0.0634$) was compared to the observed R^2, as illustrated in Figure S2.

The observed R^2 (0.9852) was significantly higher than the mean permuted R^2 ($p < 0.0001$), confirming that the monotonic decay pattern is statistically robust and not a random artifact. This result validates the use of the logistic function as a stable and meaningful empirical baseline distribution for the subsequent reliability-inspired limit state analysis.

3.3. Uncertainty Propagation via Monte Carlo Simulation

To evaluate classification stability under parameter uncertainty, 10,000 Monte Carlo simulations were executed. For the function $g_i=N_i-f(x_i,L,k,x_0)$, it was assessed to determine the probability of negative deviation ($P_{neg}=P(g_i< 0)$). The calculated P_{neg} values and 95% confidence intervals obtained from binomial normal approximations are presented in **Figure 3**. The study divided the 26 variables into 13 core symptoms and 13 peripheral manifestations using a criterion of $P_{neg} < 0.50$ (equivalent to Standardized Classification Index $\beta > 0$).

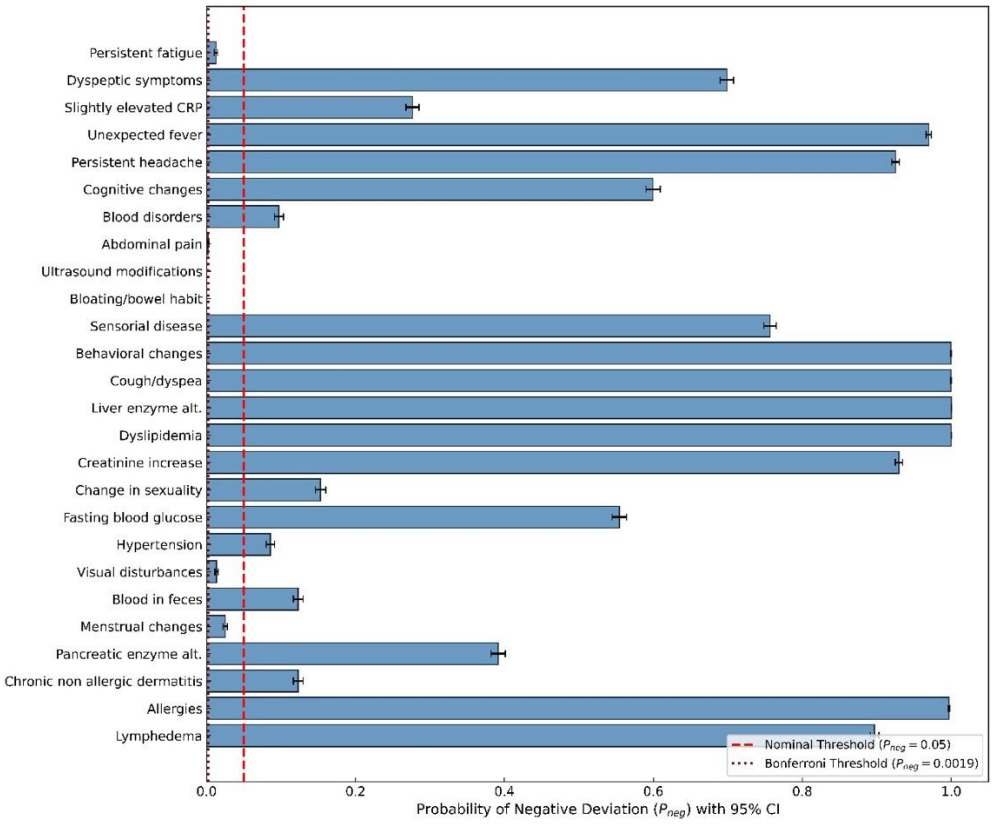

Figure 3. P_{neg} for each evaluated clinical manifestation with 95% confidence intervals.

The core symptoms showing the highest stability included persistent fatigue (P_{neg}= 0.0125, 95% CI: 0.010–0.015), ultrasound modifications (P_{neg}< 0.0001), bloating/bowel habit changes (P_{neg}< 0.0001), abdominal pain (P_{neg}< 0.0002), and visual disturbances (P_{neg}< 0.0133). Conversely, symptoms such as liver enzyme alteration (P_{neg}= 1.000), cough/dyspnea (P_{neg} = 0.9995), and allergies (P_{neg}= 0.996) consistently fell below model expectations, confirming their disease-specific or secondary nature.

The spatial distribution of points relative to the parity line reveals a systematic pattern. Symptoms positioned above the line (N > f(x), corresponding to g > 0) exhibit observed frequencies that statistically exceed model predictions, thereby qualifying as mathematically prioritized manifestations within the hypothesized clinical cluster. These points are predominantly colored green and include persistent fatigue (rank 1, N= 26$), slightly elevated CRP (rank 3, N= 22), blood disorders (rank 7, N= 16), abdominal pain (rank 8, N= 15), ultrasound modifications (rank 9, N= 15), and bloating/bowel habit changes (rank 10, N= 13). Conversely, symptoms located below the diagonal (N < f(x), corresponding to g < 0) display observed frequencies that fall short of model expectations and are classified as peripheral manifestations. These points appear in red and include dyspeptic symptoms (rank 2, N= 23), unexpected fever (rank 4, N= 19), persistent headache (rank 5, N= 18), cognitive changes (rank 6, N= 17), and sensorial disease (rank 11, N= 10).

Notably, several symptoms cluster in close proximity to the parity line, reflecting high classification uncertainty. These boundary cases, such as fasting blood glucose increase (rank 18, P_{neg}= 0.554) and cognitive changes (rank 6, P_{neg}= 0.599), are represented by yellow-to-orange hues, indicating P_{neg}values near the critical threshold of 0.5. The systematic deviation of certain high-frequency symptoms (i.e., dyspeptic symptoms at rank 2) below the predicted line suggests that while these manifestations are common across diseases, their prevalence does not exceed the baseline expectation established by the logistic model, thereby challenging their designation as syndrome-defining features.

As detailed in Supplementary Table S2 (Comprehensive Probabilistic Classification of the 26 Clinical Manifestations), manifestations such as persistent headache ($P_{neg} = 0.925$) and cognitive changes ($P_{neg} = 0.599$) did not exceed the baseline model predictions and are classified as below-baseline. Similarly, slightly elevated CRP ($P_{neg} = 0.276$) demonstrated only moderate, non-significant separation from the baseline curve.

3.4. Probabilistic Classification Analysis

Application of the probabilistic classification framework yielded Standardized Classification Indices ($\beta_i = -\Phi - 1(P_{neg,i})$) for each of the 26 clinical manifestations, providing a symmetric, dimensionless metric for evaluating deviation from the empirical baseline (Figure 4).

To control for multiplicity across the 26 evaluated manifestations, a stringent Bonferroni Bonferroni correction was applied ($\alpha = 0.05/26 \approx 0.0019$, corresponding to $\beta > 3.09$). Following this correction, two manifestations met the threshold for Robustly Above–Baseline classification: ultrasound modifications ($P_{neg} \approx 0.0000$, 95% CI: 0.0000–0.0000, $\beta = 4.75$) and bloating/bowel habit changes ($P_{neg} \approx 0.0000$, 95% CI: 0.0000–0.0000, $\beta = 4.75$).

Four additional manifestations exhibited nominal statistical significance ($P_{neg} < 0.05$) but did not survive the Bonferroni correction, qualifying as Nominally Above–Baseline: persistent fatigue ($P_{neg} = 0.0125$, 95% CI: 0.0103–0.0147, $\beta = 2.24$), abdominal pain $P_{neg} = 0.0020$, 95% CI: 0.0011–0.0029, β=2.88), visual disturbances $P_{neg} = 0.0133$, 95% CI: 0.0111–0.0155, $\beta = 2.22$), and menstrual changes ($P_{neg} = 0.0248$, 95% CI: 0.0218–0.0278, $\beta = 1.96$).

Conversely, manifestations that failed to exceed the baseline expectation were classified as Below–Baseline or Indeterminate (as detailed in Supplementary Table S2). Notably, high-prevalence features such as dyspeptic symptoms (P_{neg}= 0.6985, β = −0.52), *cognitive changes* (P_{neg}= 0.5994, β = −0.25), *persistent headache* (P_{neg}= 0.9251, β = −1.44), and *slightly elevated CRP* (P_{neg}= = 0.2763, β = 0.59) did not achieve statistical separation above the fitted baseline curve. Organ-specific markers such as *acute liver enzyme alterations* (P_{neg}=1.0000, β=−4.75), *behavioural changes* (P_{neg}=0.9995, β=−3.29), and cough/dyspnea (P_{neg}=0.9995, β=−3.29) consistently fell

below model expectations across Monte Carlo iterations. These statistical classifications purely reflect relative frequency deviations within the literature-derived matrix and do not establish biological centrality, causality, or individual MNP exposure

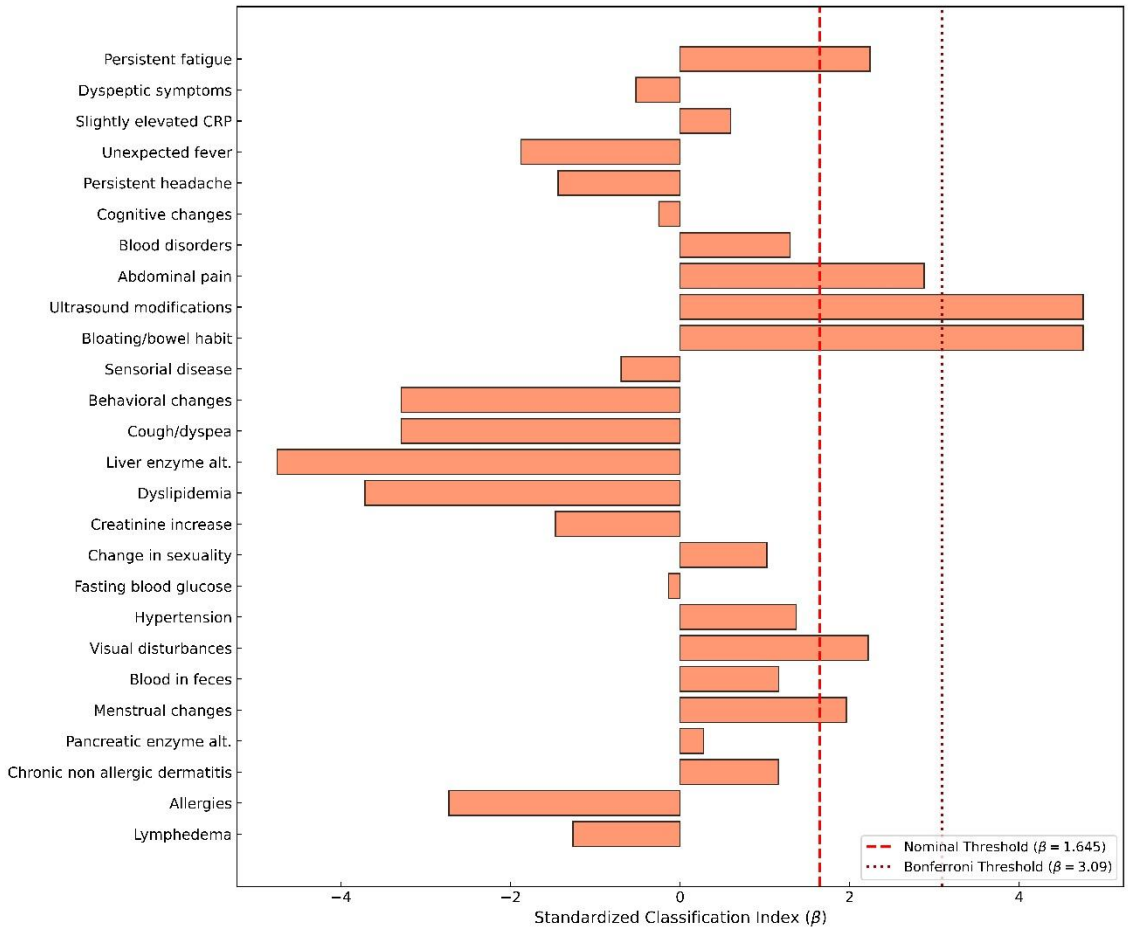

Figure 4. Standardized Classification Index (β) across clinical manifestations. Positive values ($\beta > 0$) indicate above-Baseline manifestations, while negative values denote peripheral features. Absolute magnitudes quantify statistical classification confidence.

The clear separation between core and below-Baseline manifestations in this plot underscores the robustness of the probabilistic classification framework.

The probability density state function g= [N−f(x)] for 6 sample manifestations is presented in **Figure 5**. below-Baseline manifestations (i.e., lymphoedema, P_{neg}= 0.90; creatinine rise, P_{neg}= 0.93) occur in the below-baseline domain (g< 0), whereas core manifestations (i.e., persistent fatigue) have

probability density mass concentrated nearly exclusively in the above-baseline domain (g> 0). Boundary cases that suggest categorisation ambiguity include cognitive alterations (P_{neg}= 0.60) straddling g= 0.

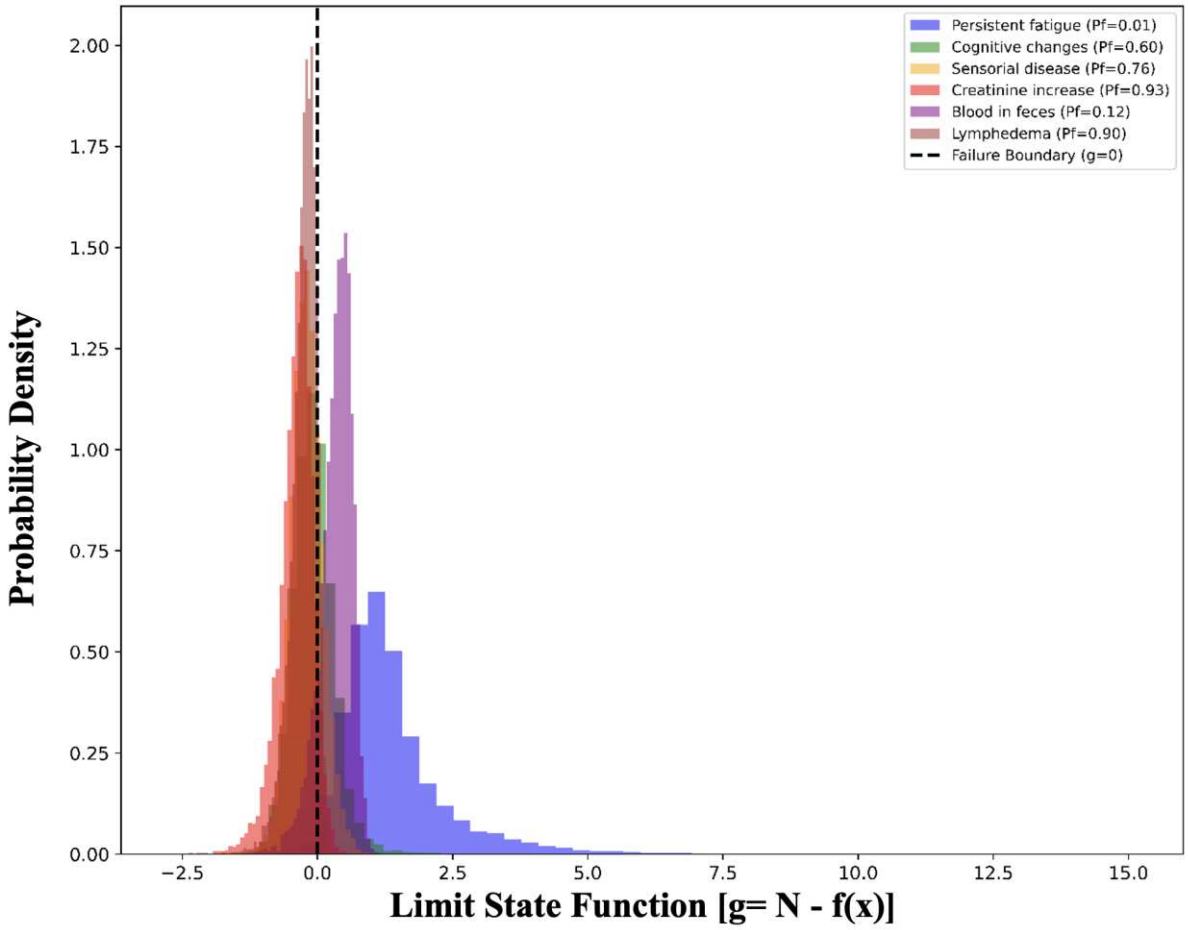

Figure 5. Probability density distributions of the limit state function g= [N−f(x)] for six representative clinical manifestations spanning the classification spectrum. The vertical dashed line (g= 0) represents the classification boundary.

The distributions of the limit state function reveal distinct patterns corresponding to symptom classification. For instance, the distribution for persistent fatigue (rank 1, P_{neg}= 0.01) is predominantly located in the positive domain (g> 0), with only a small left tail crossing the failure boundary, reflecting the high confidence in classifying this symptom as a core manifestation. In contrast, the distribution for blood in stools (rank 21, P_{neg}= 0.12) is centered in the positive domain but exhibits a more pronounced left tail, indicating moderate uncertainty in classification. The distribution for cognitive changes (rank 6, P_{neg}= 0.60) straddles the failure boundary, with substantial probability mass on both sides; this reflects the high classification uncertainty and explains why this symptom is classified as peripheral

despite its relatively high observed frequency (N=17). Moving towards the peripheral manifestations, the distribution for sensorial disease (rank 11, P_{neg}= 0.76) is predominantly located in the negative domain, with only a small right tail crossing into the above-baseline domain. Finally, the distributions for creatinine increase (rank 16, P_{neg}= 0.93) and lymphedema (rank 26, P_{neg}= 0.90) are almost entirely located in the below-baseline domain (g< 0), reflecting the high confidence in classifying these symptoms as peripheral manifestations. Overall, this visualization demonstrates how the limit state function framework captures not only the binary classification outcome but also the continuous spectrum of uncertainty inherent in symptom classification, providing a more nuanced understanding than deterministic threshold-based approaches.

3.5. Global Sensitivity Analysis (PRCC)

Partial Rank Correlation Coefficients (PRCC) were calculated to quantify the independent influence of each fitted logistic parameter (L, k, x_0) on the probabilistic classification output P_{neg}, while controlling for multi-collinearity among the parameters. PRCC is specifically employed in this context because it effectively isolates the contribution of each parameter by partialling out the linear effects of the other, potentially correlated inputs—a critical feature given that optimized parameters from nonlinear curve fitting typically exhibit non-zero covariance.

Figure 6 illustrates the PRCC values for L, k, and x_0 across all 26 clinical manifestations. The mean absolute values across all manifestations were $|\,PRCC_k\,| = 0.657$, $|\,PRCC_{x_0}\,| = 0.615$, and $|\,PRCC_L\,| = 0.576$, indicating that the decay steepness parameter (k) exerts the primary influence on overall classification uncertainty. The sensitivity analysis revealed clear rank-dependent patterns in how parameter uncertainty propagates to classification outcomes:

- **High-frequency manifestations (Ranks 1–6):** Influenced primarily by the upper asymptote L ($PRCC_L$*=0.41-0.67*).
- **Mid-frequency manifestations (Ranks 7–16):** Positively governed by L (0.58–0.58–0.74–0.74) and increasingly by k (0.12–0.12–0.87–0.87).
- **Low-frequency manifestations (Ranks 17–26):** Predominantly driven by the steepness parameter k ($PRCC_k$*=0.89–0.980.98*) and the inflection point x_0 (PRCCx0=−0.079–0.89).

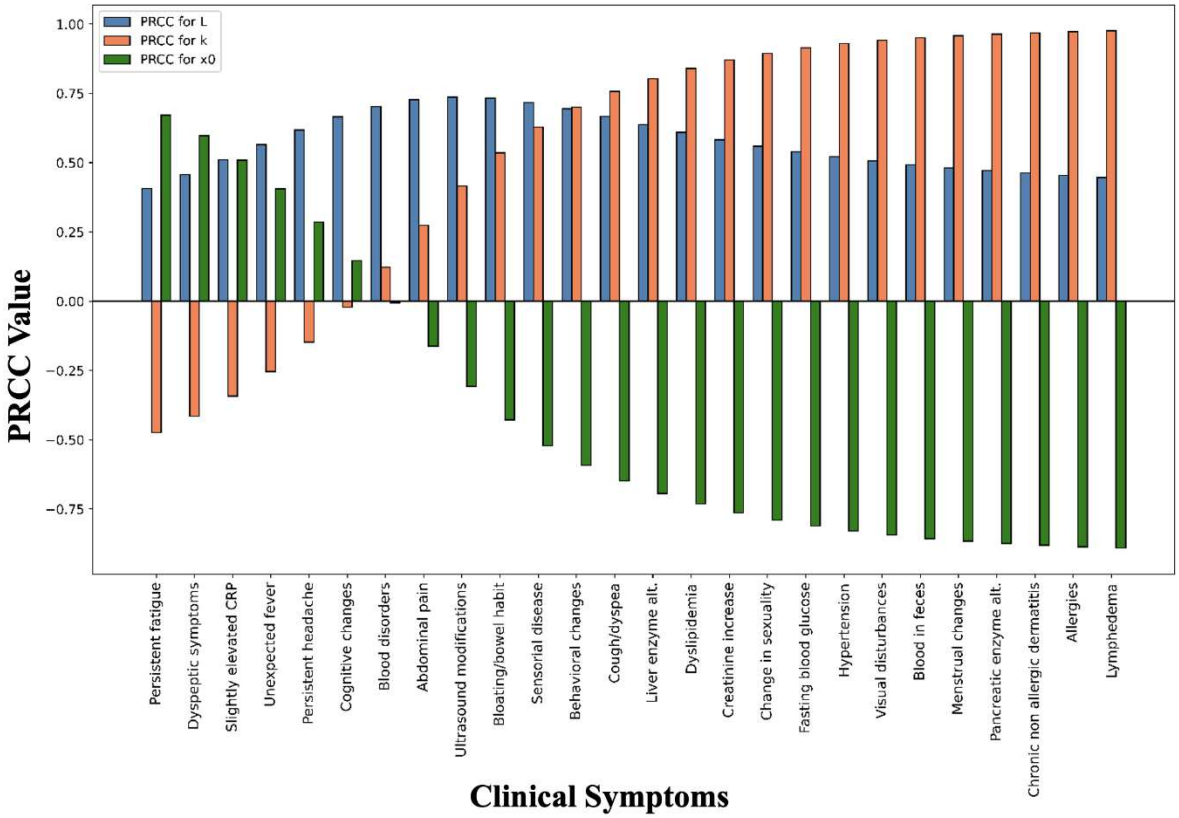

Figure 6. Global sensitivity analysis displaying PRCC for the three logistic model parameters (L, k, x_0) across all 26 clinical manifestations.

It is crucial to emphasize that this PRCC analysis exclusively quantifies the mathematical sensitivity of the symptom classification to the fitted logistic parameters (L,k,x_0). It does not establish causal links to environmental or toxicological variables (e.g., particle size, polymer composition, or additive leaching), as these exposure variables are not empirically included in the current model. The identification of k and x_0 as primary drivers for low-frequency symptoms reflects the mathematical structure of the logistic function, not an evaluated toxicological mechanism.

3.6. Phenotypic Convergence and Internal Consistency

By integrating non-linear logistic curve fitting, Monte Carlo uncertainty propagation, Bonferroni-corrected limit-state evaluation, and global sensitivity analysis, the probabilistic framework systematically ranked the 26 clinical manifestations based on their statistical deviation from the baseline model. After applying rigorous multiple-testing adjustments, alterations in ultrasonography and changes in bloating/bowel habits exhibited the most significant above-baseline categorisation (β=4.75). Characteristics exhibiting nominal significance above the baseline encompassed enduring tiredness

586 (β=2.24), gastrointestinal discomfort (β=2.88), visual impairments (β=2.22), and alterations in
587 menstruation patterns (β=1.96). Conversely, attributes including cognitive alterations, chronic
588 headaches, and marginally increased CRP did not significantly surpass baseline model anticipations and
589 were categorised as below-baseline or indeterminate (Supplementary Table S2).

590 The consistent identification of these specific manifestations across the probabilistic framework
591 indicates that their prioritization is driven by the mathematical structure of the frequency distribution
592 rather than random variation. These findings provide a reproducible mathematical basis for prioritizing
593 variables in future epidemiological studies, without implying biological validation or causality. The
594 differential sensitivity patterns across symptom ranks reveal an important mathematical insight: early-
595 ranked manifestations (high frequency) are most sensitive to the asymptotic maximum L, while late-
596 ranked manifestations (low frequency) are predominantly influenced by the steepness parameter k and
597 inflection point x_0. This reflects the inherent mathematical structure of the logistic function, where the
598 upper asymptote governs the classification uncertainty of high-frequency manifestations, while the slope
599 and inflection point determine the probabilistic boundaries for low-frequency manifestations near the
600 tail of the distribution. This structured mathematical hierarchy provides a reproducible data-driven
601 baseline for prioritizing candidate variables in future prospective epidemiological studies, without
602 implying biological validation or clinical causality.

603 **3.7. Sensitivity Analysis for Disease Selection Bias**

604 To address potential concerns regarding circularity or selection bias in disease inclusion, a
605 stratified "Leave-One-Class-Out" (LOCO) sensitivity analysis was performed. The 40 diseases were
606 grouped into major clinical classes based on the CCES framework (i.e., neurological, infectious,
607 gastrointestinal, and autoimmune). The entire probabilistic framework (logistic curve fitting and Monte
608 Carlo simulation) was systematically re-run multiple times, each time excluding one entire disease class
609 (e.g., excluding all 7 neurological diseases, then excluding all 6 infectious diseases, etc.).

610 The results of this analysis (detailed in Supplementary Material S2) demonstrated remarkable
611 stability. The symptoms identified as "Core" in the primary analysis, specifically persistent fatigue,
612 elevated inflammatory markers (CRP), gastrointestinal alterations, and abdominal discomfort,
613 consistently maintained a probability of negative deviation (P_{neg}) well below the 0.50 threshold across

all exclusion scenarios. This indicates that the identification of core manifestations is a robust, emergent property of the broader multisystemic disease spectrum, rather than an artifact driven by the overrepresentation of any single disease category.

4. Discussion

4.1. Methodological and Conceptual Evolution from the 2025 CCES Framework

The CCES framework, which originally was proposed by Cornelli et al. (2025), is specifically improved onto in this study. In order to establish a cohesive working phenotype defined as the "Microplastic Syndrome" (MSy), the original CCES provided a pioneering qualitative synthesis that included diverse clinical, laboratory, and radiological evidence. Nevertheless, since it lacked the quantitative processes required to rank manifestation dominance or systematically transmit empirical uncertainty, that original model was essentially descriptive.

By adding a rigorous mathematical and probabilistic layer to the clinical baseline, the current study improves and enhances the CCES. Our methodology extends the area from qualitative observation to quantitative prioritisation by combining logistic probability modelling, Monte Carlo uncertainty propagation, and structural reliability theory. Additionally, our reliability-inspired limit state formulation ($g = N - f(x)$ provides a mathematical framework for assessing the internal statistical consistency of the hypothesized clinical cluster as an integrated set of manifestations, while traditional clinical analyses typically assess individual symptoms separately as binary outcomes. Our logistic fit's high coefficient of determination ($R^2 = 0.9852$) indicates that the symptom frequency distribution within the selected disease spectrum follows a smooth, monotonic decay pattern that can be effectively described by a logistic function, providing a stable baseline for subsequent reliability analysis. In addition, as a consequence, this study provides a suitable methodological extension to establish internal statistical robustness and direct future epidemiological studies, but it does not replace the CCES.

4.2. Comparison with Recent MNP Studies

Our findings correspond to full agreement with the fast-increasing amounts of studies on human MNP bioaccumulation and exposure quantification (Cox et al., 2019; Mohamed Nor et al., 2021) and provide a mathematical framework for it. Peripheral blood, pulmonary tissue, hepatic parenchyma, renal

cortical structures, vascular thrombi, placental membranes, and brain tissue are only a few of the human tissues that analytical toxicologists have identified plastic particles in over the last ten years (Casella and Ballaz, 2024; Cornelli et al., 2026a; Marfella et al., 2024; Roslan et al., 2024).

Our probabilistic methodology assesses systemic phenotypic convergence, whereas previous studies have mostly concentrated on localised tissue burdens, food consumption estimations, or single-organ toxicities (Cox et al., 2019; Winiarska et al., 2024). Ingested or inhaled MNPs induce systemic oxidative stress, mitochondrial degradation, endocrine disturbances, and cellular barrier disintegration, according to recent experimental and epidemiological research (Das, 2023; Fan and Ha, 2025; Kannan and Vimalkumar, 2021; Li et al., 2023). The symptoms mathematically prioritized as 'core' in our framework, including inflammatory markers and neurological manifestations, are consistent with clinical observations reported in recent MNP bioaccumulation studies (Marfella et al., 2024). However, this consistency does not establish causality and should be interpreted as a hypothesis-generating observation warranting further prospective investigation. Our approach provides a mathematical bridge between environmental epidemiology and reliability engineering methodology, offering a framework for prioritizing variables for future toxicological investigation.

4.3. Future Mechanistic Hypotheses for Prospective Investigation

NLRP3 inflammasome activation, intestinal permeability, oxidative stress, and blood-brain barrier disruption were neither measured nor demonstrated in this study; rather, they represent mere external hypotheses to be tested in the future using direct toxicokinetic data.

The probabilistic framework presented in this study is purely empirical and mathematical. No biological, toxicological, or exposure-related mechanisms were measured or demonstrated by the data in this study. The subsequent discussion (Sections 4.3.1–4.3.4) regarding potential pathways (e.g., NLRP3 inflammasome activation, intestinal permeability, or polymer-specific leaching) represents strictly untested hypotheses that are plausibly described in the external literature. These hypotheses are proposed here solely to guide the design of future empirical studies and should not be interpreted as explanations for the mathematical results or the symptom rankings generated by the current model (Ma et al., 2022; Nemati et al., 2025).

668 It is crucial to emphasize that the classification of symptoms as 'core' in this study is a
669 mathematical prioritization based on frequency deviation from a baseline model, not a biological
670 validation. The following mechanistic discussions are strictly hypothetical explorations of how MNP
671 exposure might theoretically produce the symptoms that our mathematical framework has prioritized,
672 and do not constitute demonstration of these mechanisms.

673 A probabilistic model must be supported by valid toxicokinetic and toxicodynamic processes
674 controlling the absorption, distribution, metabolism, excretion, and toxicity (ADME-T) of plastic
675 particles in order to gain clinical credibility (Wu et al., 2022). MNPs penetrate the systemic circulation
676 by transcellular transport, persorption, or paracellular diffusion after being inhaled or consumed. These
677 particles accumulate preferentially in immunologically active organs such the liver, spleen, and vascular
678 endothelium after becoming accessible. This bio-distribution is dependent on size and surface charge
679 (Casella and Ballaz, 2024). MNP accumulation promotes lysosomal membrane permeabilization,
680 mitochondrial malfunction, persistent low-grade inflammation, and unchecked production of reactive
681 oxygen species (ROS) at the cellular level. Our reliability analysis's ability to objectively differentiate
682 between "peripheral" disease-specific noise ($\beta < 0$, $P_{neg} \geq 0.50$) and "core" systemic symptoms ($\beta > 0$,
683 $P_{neg} < 0.50$) is one of its main advantages. Systemic endothelial damage, systemic metabolic
684 dysregulation, and chronic immunological fatigue are examples of ubiquitous biochemical stress
685 responses that manifest in a variety of patient profiles and are represented by core clusters. Below-
686 Baseline manifestations, conversely, are unique downstream consequences or pre-existing comorbidities
687 that do not consistently have a mechanical connection to the internal plastic particle burden.

688 Within the probabilistic framework, persistent fatigue was classified as a nominally above-
689 baseline manifestation (β=2.24, $Pneg$=0.0125), while mildly increased C-reactive protein (hs-CRP)
690 demonstrated moderate, indeterminate separation from the baseline curve (β=0.59, $Pneg$=0.276). As
691 emphasized in the introduction to Section 4.3, the following discussion represents strictly untested
692 hypotheses regarding how MNP exposure might theoretically produce these prioritized symptoms,
693 rather than mechanisms demonstrated by the current mathematical model.

Theoretically, the biological prioritization of persistent fatigue and systemic inflammatory markers could be linked to the collapse of the intestinal barrier, macrophage-mediated systemic inflammation, and persistent oxidative stress caused by reactive oxygen species (ROS) (Das, 2023; Fan and Ha, 2025). Upon prolonged hypothetical intake, MNPs may induce mechanical abrasion and biochemical corrosion of the gastrointestinal epithelium, potentially altering mucosal tight junction proteins (i.e., zonula occludens-1, occludin) (An and Kim, 2024; Casella et al., 2025a). Both plastic particles and gut-derived lipopolysaccharides (LPS) could theoretically migrate into the portal and systemic circulation as a result of this barrier failure (Wu et al., 2022). After entering the systemic circulation, circulating monocytes and resident tissue macrophages might phagocytose MNPs. The hypothetical incapacity to degrade synthetic polymers enzymatically could lead to "frustrated phagocytosis," which may cause the NLRP3 inflammasome to remain activated, pro-inflammatory cytokines (IL-1β, IL-6, TNF-α) to be continuously released, and hepatic transcription of hs-CRP to increase (Fan and Ha, 2025). The clinical predominance of persistent fatigue and systemic inflammatory markers in future MNP cohorts might theoretically be explained by chronic low-grade cytokine activation, which could systemically cause central nervous system neuroinflammation, microglial activation, and mitochondrial bioenergetic failure (Cornelli et al., 2026). However, it must be reiterated that these pathways remain purely speculative until validated by prospective studies with quantified internal MNP burdens.

Conversely, acute alterations to hepatic enzymes (β= -4.75, P_{neg}= 1.000) were categorised as below-baseline manifestations. From a toxicological standpoint, acute serum transaminase elevations (ALT/AST) indicate short-term, dose-dependent acute injuries rather than chronic, steady-state morphology, even though the liver is the main bioaccumulative sink for systemic MNPs via the portal system (Roslan et al., 2024; Wu et al., 2022). The unique signal of MNP-induced hepatotoxicity is diluted in real-world human populations by background statistical noise, which may be attributed to dietary changes, alcohol intake, metabolic syndrome, and xenobiotic medication. The ability of our approach to identify systemic, multi-organ signals and filter out secondary clinical noise is demonstrated by the categorisation of hepatic enzyme spikes as peripheral.

Clinical presentation is mostly determined by particle size, chemical composition, and total lifetime accumulation from the standpoint of environmental toxicity (Mohamed Nor et al., 2021; Wu et al., 2022). The dynamic toxicological variables in our model are represented by the parameters L (maximum asymptote) and k (decay steepness). In particular, particle size distribution and cumulative lifetime bioavailability control parameter L, which establishes the maximum saturation frequency of above-baseline manifestations (Mohamed Nor et al., 2021). NPs exhibit exponentially greater surface-area-to-volume ratios, whereas larger MPs mostly induce localised physical discomfort in the stomach or lungs. These NPs actively penetrate placental membranes and the blood-brain barrier (BBB) by receptor-mediated transcytosis or passive permeation, creating biomolecular coronas in plasma (Bayattork et al., 2026; Bhattacharyya et al., 2025; Casella and Ballaz, 2024; Dibbon et al., 2024; Kopatz et al., 2023). Due to broad tissue permeability, parameter L rises in exposure situations dominated by NPs or high occupational doses, moving below-baseline manifestations into the core phenotypic.

Conversely, parameter k regulates the rank-decay curve's steepness and corresponds to the exposure matrix's chemical heterogeneity. Pure, pristine polymers (such as pure polystyrene-PS microbeads) generate a steep decay curve (high k) by causing predictable, organ-specific physical stress. Conversely, actual environmental plastics act as a "Trojan horse," leaching hazardous additives such as organophosphate flame retardants, phthalates, and bisphenol A (BPA) along with sorbed heavy metals that cause more extensive endocrine and metabolic disruption (Campanale et al., 2020; Kannan and Vimalkumar, 2021). Exposure to complex environmental plastic compounds mathematically flattens the rank curve, leading to a wider range of high-probability clinical symptoms and a lower k value (Zeng et al., 2026).

The current probabilistic framework treats the clinical phenotype as an aggregated outcome, without differentiating between specific polymer types (e.g., PE, PP, PET, PS, PVC) or morphologies (e.g., microfibers vs. fragments). In real-world scenarios, human populations are exposed to complex mixtures with varying translocation dynamics and chemical vector effects (Kabir et al., 2018; Kim and Liu, 2020; Zeng et al., 2026). While high-aspect-ratio nanoparticles or additive-rich weathered plastics may theoretically induce more severe systemic or metabolic disruptions, our mathematical model cannot quantify these differential effects. Future iterations of this framework must integrate polymer-specific

hazard quotients and direct internal exposure biomarkers to move beyond abstract mathematical parameters toward mechanistic, exposure-response risk assessment.

4.4. Clinical and Public Health Implications

This paradigm provides a useful conceptual foundation for clinical epidemiology and environmental health research, while being strictly intended as a hypothesis-generating analytical tool rather than a point-of-care diagnostic test or a risk assessment instrument. Future prospective cohort studies may prioritize investigating candidate phenotypes that demonstrated statistical deviation in our model, such as persistent fatigue, abdominal pain, visual disturbances, and gastrointestinal alterations (e.g., bloating/bowel habit changes), to maximize signal-to-noise ratios. However, validating these manifestations as true biomarkers strictly requires study designs that incorporate quantified internal MNP burdens and appropriate unexposed or comparator populations, which the current mathematical framework cannot provide.

Additionally, to incrementally enhance population-level research, the probabilistic framework provides a scalable matrix that could potentially incorporate emerging internal exposure biomarkers, such as circulating MNP mass concentrations, mass spectrometry-based metabolomic signatures, and specific oxidative stress indicators (Das, 2023; Wardani et al., 2024). Ultimately, future validated versions of this framework could potentially assist public health researchers in structuring targeted biomonitoring strategies for highly exposed groups, such as workers in plastic recycling facilities, workers in synthetic textiles, and coastal populations that consume large amounts of seafood (Li et al., 2025; Nguyen et al., 2025). Nevertheless, it must be emphasized that establishing evidence-based exposure thresholds or informing regulatory safety margins strictly requires prospective epidemiological data with quantified internal MNP burdens and formal toxicological risk assessments, which are beyond the scope of the current study.

4.5. Caution Regarding Regulatory and Policy Applications

The mathematical framework and standardized classification indices (β) developed in this study cannot support the derivation of Health-Based Guidance Values (HBGVs), regulatory exposure limits, or direct public health policies.

There is substantial regulatory interest in developing quantitative frameworks to characterize the potential human health impacts of microplastic and nanoplastic (MNP) exposure. Regulatory agencies, including the World Health Organization (WHO), the US Environmental Protection Agency (US EPA), and the European Chemicals Agency (ECHA), are increasingly requiring robust human risk characterizations to support policy decisions under international initiatives such as the UN Plastics Treaty (Casella et al., 2024; MacLeod et al., 2021; Stoett et al., 2024).

However, it is imperative to clarify that the mathematical framework and the resulting standardized classification indices (β) presented in this study cannot currently support the derivation of Health-Based Guidance Values (HBGVs), regulatory surveillance, or direct public health policies. Such regulatory applications strictly require robust exposure-response relationships, toxicological points of departure, reference doses, critical internal concentrations, uncertainty factors, and comprehensive population risk assessments, none of which are captured by a literature-derived symptom-disease matrix.

As a very cautious observation, future studies could test whether a model of this kind might have any utility in structuring biomonitoring efforts or informing risk assessment frameworks, but only after rigorous epidemiological validation and the integration of quantified internal MNP exposure data. Until such empirical data are available, the current framework should be viewed strictly as a hypothesis-generating mathematical tool rather than a regulatory decision-support system.

Regulatory decision-making necessitates strong exposure-response correlations, empirical points of departure, reference dosages, key internal tissue thresholds, and formal assessments of population risk. Due to the absence of matched individual-level exposure-outcome data or unexposed control cohorts in the foundational matrix, any use of these results for regulatory risk evaluation would be hasty and scientifically incorrect.

4.6. Study Limitations and Future Directions

The conclusions of this study must be interpreted in light of several fundamental structural limitations:

- Absence of Exposure and Individual Data: The unit of analysis is the disease category (N=40), not the individual participant. The dataset lacks individual-level measurements

of MNP burdens, exposure contrasts, unexposed control groups, and longitudinal follow-up. Consequently, it is mathematically impossible to estimate epidemiological metrics such as odds ratios, relative risks, or attributable fractions, or to prove an MNP-associated clinical phenotype.

- Binary Matrix Abstraction and Selection Criteria: Disease selection required the presence of at least six CCES-compatible manifestations, which inherently enriches the matrix for multisystemic overlap. Although our LOCO sensitivity analysis confirmed classification stability across disease classes, binary coding ($x_{i,j} \in \{0,1\}$) oversimplifies continuous clinical severity, duration, and dose-response dynamics.
- Non-Specific Nature of Prioritized Manifestations: Core manifestations such as persistent fatigue, abdominal pain, and elevated CRP are highly non-specific and susceptible to substantial background variation caused by lifestyle, diet, metabolic comorbidities, and environmental co-exposures (e.g., ambient fine particulate matter PM2.5 or heavy metals).
- Scope of Uncertainty Propagation: The Monte Carlo simulation propagated parameter uncertainty from the logistic curve fitting but did not quantify epistemic uncertainties arising from literature ascertainment, binary coding choices, terminology harmonization, or disease prevalence variations. Thus, the reported confidence intervals represent parameter uncertainty bounds rather than total uncertainty.
- Analytical Limits of NP Detection: Current tissue analytical techniques (i.e., Py-GC/MS, Raman microscopy) face resolution limits at the nanoscale, forcing reliance on microplastic data or chemical proxies. The manifestations mapped here cannot be linked to specific particle sizes, shapes, or chemical compositions.

A significant limitation of the current uncertainty quantification framework is that the Monte Carlo simulation propagates only parameter uncertainty from the logistic model fitting. Much larger sources of uncertainty, including disease selection criteria, symptom ascertainment from heterogeneous literature sources, binary coding decisions, terminology harmonization assumptions, variations in

disease prevalence, and study-level heterogeneity, remain unquantified. Consequently, the reported 95% confidence intervals for P_f should be interpreted strictly as parameter uncertainty bounds rather than comprehensive uncertainty estimates. Future iterations of this framework should incorporate Bayesian hierarchical models or multi-level Monte Carlo approaches to propagate these epistemic uncertainties and provide more realistic confidence intervals that reflect the full complexity of the underlying evidence base.

To ensure the robustness of these findings against selection bias and symptom heterogeneity, comprehensive sensitivity analyses (Leave-One-Disease-Out, Leave-One-Class-Out, Domain-Specific, and PCA) were performed, confirming the stability of the core symptom classification (see Supplementary **Figures S3–S6**).

Furthermore, while the logistic model provides an excellent empirical fit to the ordered data (R^2=0.9852), this high coefficient of determination reflects mathematical consistency rather than biological organization and should not be interpreted as proof of a non-random clinical phenotype.

While the 26 clinical manifestations exhibit moderate pairwise correlations (as detailed in the Correlation Matrix and PCA in Supplementary **Figures S5 and S6**), they do not demonstrate perfect semantic redundancy. Therefore, treating their aggregate frequencies as distinct points to define the empirical baseline distribution is methodologically justified for this exploratory framework.

Additionally, the Monte Carlo simulation propagated only the parameter uncertainty of the fitted logistic curve. The observed symptom frequencies (N_i) were treated as fixed values, meaning the model does not capture the epistemic uncertainty inherent in literature-derived counts, disease coding, or population prevalence.

Finally, it is imperative to clarify that the proposed mathematical framework does not represent risk attributable to MPs or NPs. The model is purely an exploratory statistical tool based on a literature-derived matrix and lacks the individual-level exposure data, dose-response relationships, and toxicokinetic parameters required for formal risk assessment. Consequently, these findings cannot and should not be used to support the development of Health-Based Guidance Values (HBGVs) or to make definitive claims regarding systemic toxicity.

Furthermore, the underlying literature used to construct the CCES matrix is inherently heterogeneous, often relying on cross-sectional designs, chemical proxies, or biomarker associations rather than direct, quantified MNP exposure data with robust confounder control. This limits the ability to draw causal inferences and underscores the necessity of treating the current findings strictly as hypothesis-generating rather than definitive clinical evidence.

Furthermore, a critical limitation of the current evidence base is the severe analytical challenge in detecting and quantifying NPs in human tissues. Current analytical techniques (i.e., Py-GC/MS, Raman microscopy) face significant sensitivity and resolution limits at the nanoscale, leading to a heavy reliance on microplastic data or indirect chemical biomarkers in human studies. Consequently, the clinical manifestations mapped in this matrix cannot be definitively attributed to specific particle sizes, shapes, or polymer types, further underscoring the need to interpret this framework strictly as a hypothesis-generating tool rather than a definitive toxicological assessment.

5. Conclusions

To advance from qualitative, descriptive categorization to rigorous quantitative prioritization in the evaluation of hypothesized clinical clusters related to MNP exposure, this study proposes a probabilistic mathematical framework. By combining nonlinear logistic curve fitting with Monte Carlo uncertainty propagation and a probabilistic limit-state formulation, the model evaluated the statistical deviation of clinical manifestations within a literature-derived symptom-disease matrix. The high goodness-of-fit (R^2=0.9852) of the baseline distribution demonstrates the internal mathematical consistency of the symptom frequency distribution within the selected disease spectrum, rather than establishing a direct biological link to MNP bioaccumulation.

From a methodological perspective, after applying a stringent Bonferroni correction for multiple comparisons, the probabilistic assessment identified a highly robust subset of manifestations—including ultrasound modifications and bloating/bowel habit changes—along with nominally significant features such as persistent fatigue, abdominal pain, visual disturbances, and menstrual changes, that exhibit the highest statistical deviation from the empirical baseline. Importantly, the global sensitivity analysis (PRCC) revealed that the classification uncertainty of low-frequency clinical outcomes is primarily

influence by the mathematical curve steepness parameter (k). This insight suggests that future prospective epidemiological studies should focus on minimizing data uncertainty in the tails of frequency distributions. Furthermore, while the mathematical boundaries conceptualized in this framework are highly dynamic, validating any theoretical relationships with environmental exposure scenarios strictly requires direct empirical data.

In conclusion, this study bridges a methodological gap by applying probabilistic mathematical frameworks to environmental epidemiology. This framework does not provide quantitative evidence of an MNP-associated phenotype, establish direct causality, or represent risk attributable to MNPs; rather, it provides public health researchers with an objective, reproducible mathematical tool to prioritize variables, design targeted biomonitoring strategies, and structure future prospective clinical cohorts. Ultimately, while this probabilistic framework serves as a robust hypothesis-generating tool, establishing direct causality and developing evidence-based clinical or regulatory guidelines will strictly require prospective longitudinal studies with validated individual-level MNP body burdens, appropriate control populations, and formal toxicological risk assessments.

6. Statements & Declarations

Credit authorship contribution statement

M. K.: Statistical analysis, Visualization, Validation, Writing original–draft; R. L.: Formal analysis, Visualization, Writing – review and editing; U. C.: Conceptualization, Visualization, Methodology, Writing original – draft, Writing – review and editing; C. C.: Conceptualization, Methodology, Visualization, Validation, Formal analysis, Supervision, Writing original–draft, Writing – review and editing.

Funding

This research was funded by the RUDN University Scientific Projects Grant System, grant number 021411-0-000.

Clinical trial number

Not applicable.

Ethical Approval

Not applicable.

Consent to Participate

Not applicable.

Consent to Publish

Not applicable.

Data Availability Statement

To ensure full transparency, reproducibility, and adherence to open science principles, all data and materials supporting the findings of this study are provided in the Supplementary Material. The complete 40 × 26 symptom-disease matrix, disease-selection rationale, binary coding decisions, optimized fitted parameters, full covariance matrix, and the complete annotated Python analysis code are available in Supplementary File S4: Data and Code Repository.

The epidemiological mortality datasets derived from ISTAT registries, along with the custom R/Python code used for the Robust Linear Regression (RLM), Huber T-norm optimization, and 5,000-iteration bootstrap simulations.

Competing Interests

The authors declare that they have no known competing financial interest or personal relationships that could have influenced the work reported in this paper.

Acknowledgements

R.L. acknowledged the support from the RUDN University Scientific Projects Grant System, grant number 021411-0-000. This article is dedicated to Alexander Santiago Casella Flores.

7. References

An YJ and Kim YH (2024) Assessment of toxicological validity using tobacco emission condensates: A comparative analysis of emissions and condensates from 3R4F reference cigarettes and heated tobacco products. Environ Int 185 108502. https://doi.org/10.1016/j.envint.2024.108502

937 Bayattork M, Rahman M, Hossain MI, Zhang Y, Haque, ANMA, Kim B, Naebe M (2026) Impact of
938 Textile-Derived Micro-and Nanoplastics on Brain Health: An Emerging Environmental Risk. Environ
939 Sci Technol https://doi.org/10.1021/acs.est.5c10338

940 Bhattacharyya S, Greer ML, Salehi M (2025) Impact of micro-and nanoplastics exposure on human
941 health: focus on neurological effects from ingestion. Front Public Health 13 1681776.
942 https://doi.org/10.3389/fpubh.2025.1681776

943 Campanale C, Massarelli C, Savino I, Locaputo V, Uricchio VF (2020) A detailed review study on
944 potential effects of microplastics and additives of concern on human health. Int J Environ Res Public
945 Health 17(4) 1212. https://doi.org/10.3390/ijerph17041212

946 Casella C, and Ballaz SJ (2024) Genotoxic and neurotoxic potential of intracellular nanoplastics: A
947 review. J Appl Toxicol 44(11) 1657-1678. https://doi.org/10.1002/jat-4598

948 Casella C, Vadivel D, Dondi D (2024) The current situation of the legislative gap on microplastics (MPs)
949 as new pollutants for the environment. Water Air Soil Pollut 235(12) 778.
950 https://doi.org/10.1007/s11270-024-07589-1

951 Casella C, Cornelli U, Ballaz S, Recchia M, Zanoni G, Ramos-Guerrero L (2025a) Preliminary study
952 on PCC-chitosan's ability to enhance microplastic excretion in human stools from healthy volunteers.
953 Foods 14(13) 2190. https://doi.org/10.3390/foods14132190

954 Chen YH, Yan C, Yang YF, Ma J X (2021) Quantitative microbial risk assessment and sensitivity
955 analysis for workers exposed to pathogenic bacterial bioaerosols under various aeration modes in two
956 wastewater treatment plants. Sci Total Environ, 755 142615.
957 https://doi.org/10.1016/j.scitotenv.2020.142615

958 Cornelli U, Casella C, Belcaro G, Cesarone MR, Marucci S, Rondanelli M, Zanoni G (2025) Definition
959 of Emerging Microplastic Syndrome Based on Clinical and Epidemiological Evidence: A Narrative
960 Review. Microplastics 4(4) 93. https://doi.org/10.3390/microplastics4040093

961 Cornelli U, Belcaro G, Casella C (2026) Reduction in Circulating Microplastics in Humans Following
962 Gastrointestinal Sequestration by Chitosan: A Pilot Controlled Study. J Xenobiotics 16(3) 92.
963 https://doi.org/10.3390/jox16030092

964 Cox KD, Covernton GA, Davies HL, Dower JF, Juanes F, Dudas SE (2019) Human consumption of
965 microplastics. Environ Sci Technol 53(12) 7068-7074. https://doi.org/10.1021/acs.est.0c04032

966 Das A (2023) The emerging role of microplastics in systemic toxicity: Involvement of reactive oxygen
967 species (ROS). Sci Total Environ 895 165076. https://doi.org/10.1016/j.scitotenv.2023.165076

968 Dibbon KC, Mercer GV, Maekawa AS, Hanrahan J, Steeves KL, Ringer LC, Cahill LS (2024)
969 Polystyrene micro-and nanoplastics cause placental dysfunction in mice. Biol Reprod 110(1) 211-218.
970 https://doi.org/10.1093/biolre/ioad126

971 Fan J and Ha Y (2025) Micro-and nanoplastics and the immune system: mechanistic insights and future
972 directions. Immuno 5(4) 52. https://doi.org/10.3390/immuno5040052

973 Kabir S, Yazdi M, Aizpurua JI, Papadopoulos Y (2018) Uncertainty-aware dynamic reliability analysis
974 framework for complex systems. IEEE Access 6 29499-29515.
975 https://doi.org/10.1109/ACCESS.2018.2843166

976 Kannan K and Vimalkumar K (2021) A review of human exposure to microplastics and insights into
977 microplastics as obesogens. Front Endocrinol 12 724989. https://doi.org/10.3389/fendo.2021.724989

978 Koelmans AA, Redondo-Hasselerharm PE, Nor NHM, de Ruijter VN, Mintenig SM, Kooi M (2022)
979 Risk assessment of microplastic particles. Nat Rev Mater 7(2) 138-152. https://doi.org/10.1038/s41578-
980 021-00411-y

981 Kopatz V, Wen K, Kovács T, Keimowitz AS, Pichler V, Widder J, Kenner L (2023) Micro-and
982 nanoplastics breach the blood–brain barrier (BBB): Biomolecular corona's role revealed. Nanomaterials
983 13(8) 1404. https://doi.org/10.3390/nano13081404

984 Kim M and Liu K (2020) A Bayesian deep learning framework for interval estimation of remaining
985 useful life in complex systems by incorporating general degradation characteristics. IISE Transact 53(3)
986 326-340. ttps://doi.org/10.1080/24725854.2020.1766729

Li Y, Tao L, Wang Q, Wang F, Li G, Song M (2023) Potential health impact of microplastics: a review of environmental distribution, human exposure, and toxic effects. Environ Health 1(4) 249-257. https://doi.org/10.1021/envhealth.3c00052

Li Y, Ling W, Yang J, Xing Y (2025) Risk assessment of microplastics in humans: distribution, exposure, and toxicological effects. Polymers 17(12) 1699. https://doi.org/10.3390/polym17121699

Liu B, Zhang Z, Wen Y, Kang S, Guo Y, Qiu Q (2020) Reliability analysis for complex systems subject to competing failure processes in an uncertain environment. J Intell Fuzzy Syst 39(3) 4331-4339. https://doi.org/10.3233/JIFS-200343

Ma Z, Li J, Zhang M, You D, Zhou,Y, Gong Z (2022) Groundwater health risk assessment based on Monte Carlo model Sensitivity analysis of Cr and As—a case study of Yinchuan city. Water 14(15) 2419. https://doi.org/10.3390/w14152419

MacLeod M, Arp HPH, Tekman MB, Jahnke A (2021) The global threat from plastic pollution. Science 373(6550) 61-65. https://doi.org/10.1126/science.abg5433

Marfella R, Prattichizzo F, Sardu C, Fulgenzi G, Graciotti L, Spadoni T, Paolisso G (2024) Microplastics and nanoplastics in atheromas and cardiovascular events. New Eng J Med 390(10) 900-910. https://doi.org/10.1056/NEJMoa2309822

Mohamed Nor NH, Kooi M, Diepens NJ, Koelmans AA (2021) Lifetime accumulation of microplastic in children and adults. Environ Sci Technol 55(8) 5084-5096. https://doi.org/10.1021/acs.est.0c07384

Mohammadpour A, Rajabi S, Bell M, Baghapour MA, Aliyeva A, Mousavi Khaneghah A (2023) Seasonal variations of potentially toxic elements (PTEs) in drinking water and health risk assessment via Monte Carlo simulation and Sobol sensitivity analysis in southern Iran's largest city. Appl Water Sci 13(12) 237. https://doi.org/10.1007/s13201-023-02041-x

Nemati B, Fallahizadeh S, Mostafaei G, Miranzadeh MB (2025) Health risk assessment of toxic elements in Kashan drinking water reservoirs using Monte Carlo simulation and sensitivity analysis. Sci Rep 15(1) 17806. https://doi.org/10.1038/s41598-025-01847-w

Nguyen MK, Lin C, Nguyen DD (2025) Microplastic pollution associated with probabilistic human health risks: Potential hazards, critical factors, challenges, and limitations. Mar Pollut Bull 221 118528. https://doi.org/10.1016/j.marpolbul.2025.118528

Plastics Europe 2025—The Fast Facts 2025 Plastics Europe (2025) Available online at https://plasticseurope.org/knowledge-hub/plastics-the-fast-facts-2025. Accessed 26 June 2026

Prata JC, Da Costa JP, Lopes I, Duarte AC, Rocha-Santos T (2020) Environmental exposure to microplastics: An overview on possible human health effects. Sci Total Environ 702 134455. https://doi.org/10.1016/j.scitotenv.2019.134455

Roslan NS, Lee YY, Ibrahim YS, Anuar ST, Yusof KMKK, Lai LA, Brentnall T (2024) Detection of microplastics in human tissues and organs: A scoping review. J Glob Health 14 04179. https://doi.org/10.7189/jogh.14.04179

Stoett P, Scrich VM, Elliff CI, Andrade MM, Grilli NDM, Turra A (2024) Global plastic pollution, sustainable development, and plastic justice. World Develop 184 106756. https://doi.org/10.1016/j.worlddev.2024.106756

Wardani I, Nor NHM, Wright SL, Kooter, IM, Koelmans AA (2024) Nano-and microplastic PBK modeling in the context of human exposure and risk assessment. Environ Int 186 108504. https://doi.org/10.1016/j.envint.2024.108504

Winiarska E, Jutel M, Zemelka-Wiacek M (2024) The potential impact of nano-and microplastics on human health: Understanding human health risks. Environ Res 251 118535. https://doi.org/10.1016/j.envres.2024.118535

Wu P, Lin S, Cao G, Wu J, Jin H, Wang C, Cai Z (2022) Absorption, distribution, metabolism, excretion and toxicity of microplastics in the human body and health implications. J Hazard Mater 437 129361. https://doi.org/10.1016/j.jhazmat.2022.129361

Zeng Z, Lin C, Peng W, Xu M (2026) The evolving paradigm of reliability engineering for complex systems: A review from an uncertainty control perspective. Aerospace 13(2) 183. https://doi.org/10.3390/aerospace13020183

1038 Zhao S, Gong Y, Yang S, Chen S, Huang D, Yang K, Cheng H (2023) Health risk assessment of heavy
1039 metals and disinfection by-products in drinking water in megacities in China: A study based on age
1040 groups and Monte Carlo simulations. Ecotoxicol Environ Saf 262 115330.
1041 https://doi.org/10.1016/j.ecoenv.2023.115330

Supplementary Files

This is a list of supplementary files associated with this preprint. Click to download.

- SupplementaryMaterialsOctober192026.docx